Lateral distributed-feedback gratings for single-mode, high-power terahertz quantum-cascade lasers

M. Wienold,[*] **A. Tahraoui, L. Schrottke, R. Sharma, X. Lü, K. Biermann, R. Hey, and H. T. Grahn**

Paul-Drude-Institut für Festkörperelektronik, Hausvogteiplatz 5–7, 10117 Berlin, Germany

[*]*wienold@pdi-berlin.de*

Abstract: We report on terahertz quantum-cascade lasers (THz QCLs) based on first-order lateral distributed-feedback (lDFB) gratings, which exhibit continuous-wave operation, high output powers (>8 mW), and single-mode emission at 3.3–3.4 THz. A general method is presented to determine the coupling coefficients of lateral gratings in terms of the coupled-mode theory, which demonstrates that large coupling strengths are obtained in the presence of corrugated metal layers. The experimental spectra are in agreement with simulations of the lDFB cavities, which take into account the reflective end facets.

References and links

1. H.-W. Hübers, S. G. Pavlov, A. D. Semenov, R. Köhler, L. Mahler, A. Tredicucci, H. E. Beere, D. A. Ritchie, and E. H. Linfield, "Terahertz quantum cascade laser as local oscillator in a heterodyne receiver," Opt. Express **13**, 5890–5896 (2005).
2. H. Richter, A. D. Semenov, S. G. Pavlov, L. Mahler, A. Tredicucci, H. E. Beere, D. A. Ritchie, K. S. Il'in, M. Siegel, and H.-W. Hübers, "Terahertz heterodyne receiver with quantum cascade laser and hot electron bolometer mixer in a pulse tube cooler," Appl. Phys. Lett. **93**, 141108 (2008).
3. P. Khosropanah, W. Zhang, J. N. Hovenier, J. R. Gao, T. M. Klapwijk, M. I. Amanti, G. Scalari, and J. Faist, "3.4 THz heterodyne receiver using a hot electron bolometer and a distributed feedback quantum cascade laser," J. Appl. Phys. **104**, 113106 (2008).
4. D. Rabanus, U. U. Graf, M. Philipp, O. Ricken, J. Stutzki, B. Vowinkel, M. C. Wiedner, C. Walther, M. Fischer, and J. Faist, "Phase locking of a 1.5 Terahertz quantum cascade laser and use as a local oscillator in a heterodyne HEB receiver," Opt. Express **17**, 1159–1168 (2009).
5. Y. Ren, J. N. Hovenier, R. Higgins, J. R. Gao, T. M. Klapwijk, S. C. Shi, B. Klein, T.-Y. Kao, Q. Hu, and J. L. Reno, "High-resolution heterodyne spectroscopy using a tunable quantum cascade laser around 3.5 THz," Appl. Phys. Lett. **98**, 231109 (2011).
6. H. Richter, M. Greiner-Bär, S. G. Pavlov, A. D. Semenov, M. Wienold, L. Schrottke, M. Giehler, R. Hey, H. T. Grahn, and H.-W. Hübers, "A compact, continuous-wave terahertz source based on a quantum-cascade laser and a miniature cryocooler," Opt. Express **18**, 10177–10187 (2010).
7. J. Faist, C. Gmachl, F. Capasso, C. Sirtori, D. L. Sivco, J. N. Baillargeon, and A. Y. Cho, "Distributed feedback quantum cascade lasers," Appl. Phys. Lett. **70**, 2670–2672 (1997).
8. G. P. Luo, C. Peng, H. Q. Le, S. S. Pei, W.-Y. Hwang, B. Ishaug, J. Um, J. N. Baillargeon, and C.-H. Lin, "Grating-tuned external-cavity quantum-cascade semiconductor lasers," Appl. Phys. Lett. **78**, 2834–2636 (2001).
9. J. Xu, J. M. Hensley, D. B. Fenner, R. P. Green, L. Mahler, A. Tredicucci, M. G. Allen, F. Beltram, H. E. Beere, and D. A. Ritchie, "Tunable terahertz quantum cascade lasers with an external cavity," Appl. Phys. Lett. **91**, 121104 (2007).
10. L. Mahler, A. Tredicucci, R. Köhler, F. Beltram, H. E. Beere, E. H. Linfield, and D. A. Ritchie, "High-performance operation of single-mode terahertz quantum cascade lasers with metallic gratings," Appl. Phys. Lett. **87**, 181101 (2005).

11. M. I. Amanti, M. Fischer, G. Scalari, M. Beck, and J. Faist, "Low-divergence single-mode terahertz quantum cascade laser," Nat. Photonics **3**, 586–590 (2009).
12. L. Mahler, A. Tredicucci, F. Beltram, C. Walther, J. Faist, H. E. Beere, and D. A. Ritchie, "High-power surface emission from terahertz distributed feedback lasers with a dual-slit unit cell," Appl. Phys. Lett. **96**, 191109 (2010).
13. D. G. Allen, T. Hargett, J. L. Reno, A. A. Zinn, and M. C. Wanke, "Index tuning for precise frequency selection of terahertz quantum cascade lasers," IEEE Photon. Technol. Lett. **23**, 30–32 (2011).
14. S. Golka, C. Pflügl, W. Schrenk, and G. Strasser, "Quantum cascade lasers with lateral double-sided distributed feedback grating," Appl. Phys. Lett. **86**, 111103 (2005).
15. B. S. Williams, S. Kumar, Q. Hu, and J. L. Reno, "Distributed-feedback terahertz quantum-cascade lasers with laterally corrugated metal waveguides," Opt. Lett. **30**, 2909–2911 (2005).
16. M. I. Amanti, G. Scalari, F. Castellano, M. Beck, and J. Faist, "Low divergence Terahertz photonic-wire laser," Opt. Express **18**, 6390–6395 (2010).
17. R. Köhler, A. Tredicucci, F. Beltram, H. E. Beere, E. H. Linfield, A. G. Davies, D. A. Ritchie, R. C. Iotti, and F. Rossi, "Terahertz semiconductor-heterostructure laser," Nature (London) **417**, 156–159 (2002).
18. M. Rochat, A. Lassaad, H. Willenberg, J. Faist, H. Beere, G. Davies, E. Linfield, and D. Ritchie, "Low-threshold terahertz quantum-cascade lasers," Appl. Phys. Lett. **81**, 1381–1383 (2002).
19. B. S. Williams, "Terahertz quantum-cascade lasers," Nat. Photonics **1**, 517–525 (2007).
20. H. Kogelnik and C. V. Shank, "Coupled-wave theory of distributed feedback lasers," J. Appl. Phys. **43**, 2327–2335 (1972).
21. S. L. Chuang, *Physics of Photonic Devices* (Wiley, New York, 2009), 2nd ed.
22. A. Laakso, M. Dumitrescu, J. Viheriälä, J. Karinen, M. Suominen, and M. Pessa, "Optical modeling of laterally-corrugated ridge-waveguide gratings," Opt. Quant. Electron. **40**, 907–920 (2008).
23. S. Kohen, B. S. Williams, and Q. Hu, "Electromagnetic modeling of terahertz quantum cascade laser waveguides and resonators," J. Appl. Phys. **97**, 053106 (2005).
24. P. Berini, "Plasmon-polariton waves guided by thin lossy metal films of finite width: Bound modes of symmetric structures," Phys. Rev. B **61**, 10484–10503 (2000).
25. M. Wienold, L. Schrottke, M. Giehler, R. Hey, W. Anders, and H. T. Grahn, "Low-threshold terahertz quantum-cascade lasers based on GaAs/Al$_{0.25}$Ga$_{0.75}$As heterostructures," Appl. Phys. Lett. **97**, 071113 (2010).
26. A. Barkan, F. K. Tittel, D. M. Mittleman, R. Dengler, P. H. Siegel, G. Scalari, L. Ajili, J. Faist, H. E. Beere, E. H. Linfield, A. G. Davies, and D. A. Ritchie, "Linewidth and tuning characteristics of terahertz quantum cascade lasers," Opt. Lett. **29**, 575–577 (2004).

1. Introduction

Terahertz quantum-cascade lasers (THz QCLs) have been proposed and demonstrated for applications such as local oscillators in heterodyne receivers [1–5] above 2 THz. This requires THz QCLs, which operate in continuous-wave (cw) mode with a high output power in a single spectral mode. Operation in a liquid nitrogen dewar or a small-size Stirling cooler is preferred [6]. The two conventional approaches for obtaining single-mode QCLs have been distributed-feedback (DFB) gratings and external-cavity setups [7, 8]. However, for THz QCLs, the realization of tunable external cavities is complicated by the limitations due to the cryogenic operating temperatures and the fabrication of THz anti-reflection coatings [9]. THz QCLs with a DFB grating are often realized by slits in the top metallization of the laser ridge [10–13], which provide a strong feedback due to the large modal intensity at the top metal and the large refractive index modulation. The electrical contacting of the laser ridges is typically performed by just one or two thin bonding wires attached to the ends of the laser ridge in order to avoid any interference with the grating slits. An alternative approach is the use of lateral DFB (lDFB) gratings [14–16], which allow for a closed top metallization such as for Fabry-Pérot THz QCLs. The advantages of lateral gratings are a homogeneous current injection and the possibility of using a larger number of bonding wires, which reduces the current load for each wire and consequently the risk of failure in the case of cw operation. THz QCLs with first-order lDFB gratings and sub-mW output powers have already been demonstrated for metal-metal waveguides [15], for which the optical mode is confined between two metal layers. In contrast, we pursue the approach of first-order lDFB gratings in combination with single-plasmon waveguides. In single-plasmon waveguides [17, 18], the optical mode is confined between the top metal and a highly *n*-doped layer underneath the active region. Fabry-Pérot lasers based on
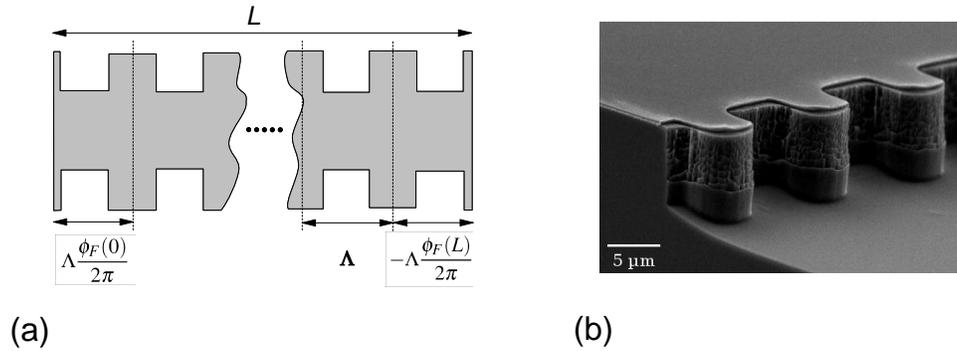
Fig. 1. (a) Schematic diagram of a THz QCL with a lDFB grating. L denotes the length of the laser, Λ the grating period, and $\phi_F(0)$ and $\phi_F(L)$ the facet phases with respect to the grating comb. (b) Scanning electron microscopy (SEM) image of an lDFB mesa after dry etching.

this type of waveguide have shown to be beneficial over metal-metal waveguides with respect to output power and beam quality [19]. Note that the lasing mode is transverse magnetically (TM) polarized in QCLs. In the first part of this paper, we present a general method to calculate the coupling strength of lDFB gratings in terms of the well established coupled-mode theory (CMT) [20]. In the second part, experimental results are discussed and compared to simulations of the lDFB cavities.

2. Modeling of lateral gratings

In a DFB grating, the dielectric function is modulated in the ridge direction (labeled z), where in the following $\Delta\varepsilon(z)$ denotes the modulation of the dielectric function with respect to a reference waveguide. In Fig. 1(a), a schematic diagram of an lDFB QCL with its two end facets is shown. The grating period Λ corresponds to the vacuum Bragg wavelength of $\lambda_B = 2\Lambda n/m$, where n denotes the real part of the effective refractive index of the waveguide ($n_{\text{eff}} = n + ik$) and m the grating order. Figure 1(b) depicts an lDFB mesa after dry etching.

   Within the CMT, the coupling coefficients describe the coupling of the forward and backward traveling waves. This section deals mainly with determining the coupling coefficients of lDFB gratings; for a comprehensive introduction to the CMT of DFB lasers, see for example Ref. [21]. The coupling coefficients of an mth-order grating are usually determined by two-dimensional integrals of the mth Fourier components of $\Delta\varepsilon$ weighted by the modal intensity profile of the corresponding reference waveguide (cf. Ref. [21]). For the integration, the change of the modal intensity profile between the two grating sections is assumed to be negligibly small. There are in general two complex coupling coefficients for the coupling of forward with backward and of backward with forward traveling waves. Here, only symmetric gratings are considered, for which the origin in the ridge direction z can be chosen such that $\Delta\varepsilon(z) = \Delta\varepsilon(-z)$. In this case, the two complex coupling coefficients can be subsumed into a single complex coupling coefficient $K + iK_g$, where the index coupling coefficient K is positive and the gain coupling coefficient K_g can be positive or negative due to a possible phase difference of 0 or π between index and gain coupling.

   In Ref. [22], the coupling coefficients for interband DFB lasers based on lateral gratings are determined by assuming a reference waveguide with an average refractive index in the lateral corrugation region. However, this approach does not account for changes of the intensity

profile of modes, which are located in different grating sections. In our case, different mode profiles in the wide- and narrow-ridge sections are caused by the presence of a corrugated metal layer. A more appropriate way to calculate the coupling coefficients in this case arises from the correspondence of uniform DFB gratings and one-dimensional photonic crystals.

The band gap of a one-dimensional photonic crystal corresponds to the stop band of a uniform DFB grating caused by the coupling of forward and backward propagating waves. It can be shown (see Appendix) that the complex coupling coefficient of a first-order symmetric grating is related to the complex eigenfrequencies $\omega_\pm$ of the lowest two bands of a one-dimensional photonic crystal at the Bragg wavevector by

$$\omega_\pm = \frac{c}{n+ik}\left[\frac{\pi}{\Lambda} \pm (K+iK_g)\right] \approx \frac{c}{n}\left[\frac{\pi}{\Lambda} \pm (K+iK_g) + i\frac{g_n}{2}\right] , \qquad (1)$$

where c denotes the speed of light. The net gain g_n is given by $g_n = \Gamma g - \alpha_w$ with Γg being the confinement factor times material gain and α_w the waveguide losses. The difference of the two eigenfrequencies corresponds to the complex coupling coefficient

$$K + iK_g = \frac{n_g}{2c}(\omega_+ - \omega_-) \qquad (2)$$

with n_g denoting the group refractive index. The problem of calculating the coupling coefficients is now shifted from a two-dimensional integration to a calculation of the complex eigenfrequencies of a photonic crystal at the Bragg wavevector. For an lDFB grating implemented in a THz waveguide, this requires to solve Maxwell's equations for the volume of the DFB unit cell with periodic boundary conditions in the z direction. We performed this task by means of a finite-element method using a commercial Maxwell solver (JCMwave, JCMsuite).

In the simple case of an index DFB grating, which consists of two alternating homogeneous slabs, i.e. a grating with a square modulation of the dielectric constant and no waveguide dispersion ($n_g = n$), the expression for K becomes a very simple analytic one:

$$K = \frac{\Delta\varepsilon}{2\Lambda n^2} = \frac{2\Delta n}{\lambda_B} , \qquad (3)$$

where $\Delta\varepsilon = 2n\Delta n$ denotes the difference of the dielectric constant between the sections. Equation (3) can be easily derived from the general Eqs. (1) and (2) cited in [22]; other derivations can be found in many textbooks (cf. citations in [15, 22]). Using $\Lambda = 12.5\ \mu$m, $\Delta\varepsilon = 0.2$, and $n = 3.584$, Eq. (3) results in $K = 6.23\ \text{cm}^{-1}$. This is exactly the same value as obtained via the numerical determination of ω_- and ω_+ for the corresponding one-dimensional photonic crystal, which confirms the validity of the photonic-crystal approach. Since a stack of homogeneous slabs is considered here, the numerical result for K does not depend on the lateral and vertical dimensions of the simulated unit cell.

Figure 2(a) depicts the geometry of the unit cell used for the calculations of the lDFB coupling coefficients; exploiting the symmetry of the problem, only half of the original grating unit cell is simulated. Modes, which are symmetric and antisymmetric with respect to the center of the ridge, are found for different boundary conditions at $x = 0$ (vanishing tangential magnetic or electric field, respectively). The grating period is 12.5 μm, and the full width of the ridge is 120 and 107 μm in the wide- and narrow-ridge section, respectively. The THz dielectric constants used in the simulations are basically the same as in Ref. [23]. However, for GaAs and $Al_xGa_{1-x}As$, we take into account the contribution of bulk phonons, and we neglect free-carrier absorption in the active region. The different panels in Fig. 2(b) show the two perpendicular projections of the modal intensity for the ω_- and ω_+ modes with the fundamental TM_{00} symmetry. The ω_+ mode is localized in the narrow-ridge section of the grating, and the mode profile is
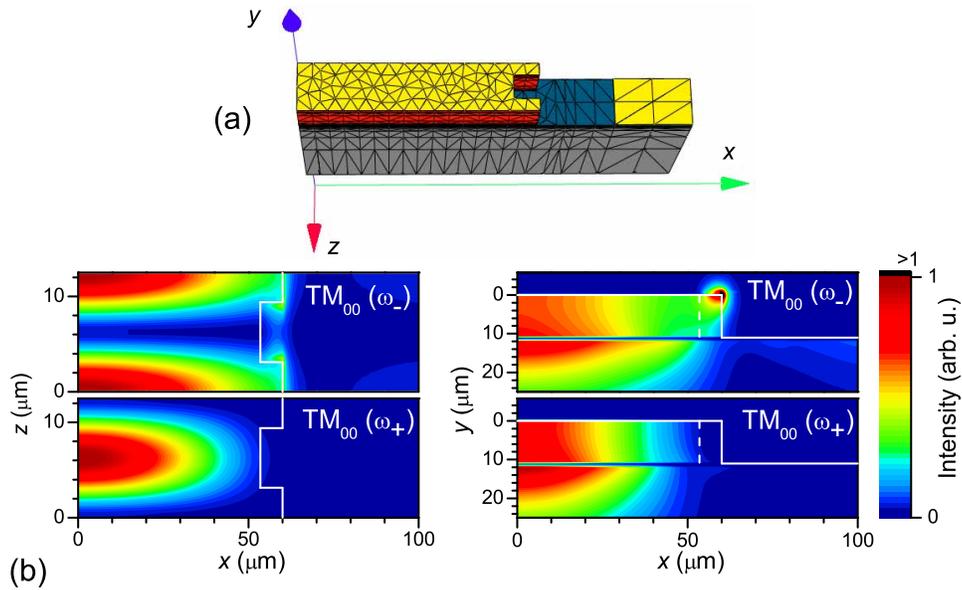
Fig. 2. (a) Geometry and initial finite-element grid of the unit cell (periodic in the *z*-direction) used in the simulation of the uniform lDFB grating. Top and bottom metallizations are yellow colored, the active region red, the highly doped bottom contact layer blue, and the substrate gray. Perfectly matched layers are applied at $x = 100$ μm (transparent boundary conditions). (b) Projections of the intensity distribution of the ω_- and ω_+ TM$_{00}$ modes to the *xz* and *xy* plane.

basically that of a Fabry-Pérot single-plasmon waveguide. The ω_- mode is localized mainly in the wide-ridge section, and the mode profile is significantly altered as compared to the ω_+ mode. The intensity distribution exhibits features of a surface plasmon bound to a metal film of finite width [24] such as the large intensity peaks, which occur at the edges of the top metallization outside the actual ridge volume. Furthermore, the ω_- mode appears to couple weakly to the bottom contact metallization.

The results for the eigenfrequencies and coupling coefficients are summarized in Table 1. The magnitude of the coupling coefficient increases strongly with increasing lateral mode index, which is related to a stronger localization of the ω_- modes at the edges of the corrugated ridge. Since the imaginary parts of ω_- and ω_+ are different, the coupling coefficient contains an imaginary component K_g. Because gain has been neglected in the simulations, i.e. $g_n = -\alpha_w$, the effective waveguide losses for the corresponding reference waveguide can be determined via $\alpha_w = \mathrm{Im}(\omega_+ + \omega_-)n/c$. A value of 11.1 cm^{-1} for the TM$_{00}$ modes is obtained, while 2D waveguide simulations of the narrow- and wide-ridge section result in 9.5 and 9.4 cm^{-1}, respectively. Hence, the lateral grating causes on average additional losses of about 1.7 cm^{-1}. The larger magnitudes of the imaginary part of $\omega_\pm$ for the TM$_{01}$ and TM$_{02}$ modes correspond to effective losses of 20 and 30 cm^{-1}, respectively, which should usually inhibit lasing in the higher-order lateral modes.

To illustrate the impact of the corrugated metal grating, we can estimate the grating coupling strength assuming the same mode profile for the ω_+ and ω_- modes. In this case, an upper limit for the coupling strength is given by Eq. (3) using $\Delta\varepsilon = n_w^2 - n_n^2$ with the effective indices n_w

Table 1. Real and imaginary part of the eigenfrequencies ω_- and ω_+ and corresponding coupling coefficient $K + iK_g$ ($n_g = 3.8$) for the TM_{00}, TM_{01}, and TM_{02} modes for the grating geometry shown in Fig. 2(a).

	TM_{00}	TM_{01}	TM_{02}
$\mathrm{Re}(\omega_-/[2\pi c])$ (cm^{-1})	110.83	111.79	113.66
$\mathrm{Re}(\omega_+/[2\pi c])$ (cm^{-1})	111.09	112.79	115.54
$\mathrm{Im}(\omega_-/[2\pi c])$ (cm^{-1})	−0.28	−0.53	−0.79
$\mathrm{Im}(\omega_+/[2\pi c])$ (cm^{-1})	−0.21	−0.34	−0.55
K (cm^{-1})	3.0	11.9	22.5
K_g (cm^{-1})	0.8	2.3	2.9

and n_n corresponding to separate two-dimensional (2D) waveguide simulations for the wide- and narrow-ridge section, respectively. By doing so, we obtain a value of $K = 0.75$ cm^{-1} for the fundamental TM_{00} mode, which is by a factor of 4 smaller than compared to the value obtained via the rigorous photonic-crystal method. Hence, the origin of the strong coupling is related to the plasmonic intensity peaks at the grating edges, which occur only for the ω_- mode [cf. Fig. 2(b)] and result in a large difference between ω_+ and ω_-.

For known coupling coefficients, the CMT allows for a determination of the complex eigenvalues of the DFB cavity, i.e. the frequencies and threshold gain for the different longitudinal modes. Note that in case of reflective end facets the cavity eigenvalues depend also on the facet phases ϕ_F [cf. Fig. 1(a)]. In the case of cleaved facets, these are not known *a priori* due to the limited accuracy of the cleaving process. This causes an uncertainty of the frequency values, which is approximately equal to the mode spacing of the corresponding Fabry-Pérot cavity.

3. Experimental results and discussion

The THz QCL active region is based on the GaAs/Al$_{0.25}$Ga$_{0.75}$As heterostructure reported as sample B in Ref. [25]. The processing is similar to single-plasmon Fabry-Pérot lasers. In the first step, the metal grating is defined in a lift-off process (10/100 nm Ti/Au). This is followed by a dry etching step to form the corrugated mesa and a second metallization/lift-off step, which defines the bottom contact and reinforces the bonding area of the top contact (300 nm AuGe/Ni). For dry etching, we used a silicon oxide hard mask and a reactive ion etch system based on an inductively coupled plasma (SAMCO RIE-140iP). The grating duty cycle is 0.5, and the widths of the wide- and narrow-ridge sections of the etched mesa are approximately 120 and 107 μm. These are also the parameters, which we used for the simulations (neglecting a small technological gap of about 1 μm between the top metallization and the etch mask).

In the following, the experimental results for three laser stripes from a single die with grating periods of 12.4, 12.5, and 12.6 μm and as-cleaved facets are discussed. The corresponding Bragg frequencies fall within the emission range of 3.15–3.45 THz found for Fabry-Pérot lasers of the same wafer. Since the three laser stripes are located on the same die, they have all the same ridge length (1.454 mm). Figure 3(a) shows the light-current-voltage (*L-I-V*) characteristics of the three lasers for driving currents up to 0.75 A (455 A cm^{-2}). In this range, the emission of the lasers is dominated by a single spectral mode. Due to the large dissipated electrical power, only temperatures above 20 K can be maintained over the whole range of driving currents. The three lasers exhibit similar *L-I-V* characteristics with threshold current densities J_{th} of 290, 290, and 270 A cm^{-2} at 30 K for $\Lambda = 12.4$, 12.5, and 12.6 μm, respectively. The maximum operating temperature is about 55 K for $\Lambda = 12.4$ and 12.5 μm and about 60 K for
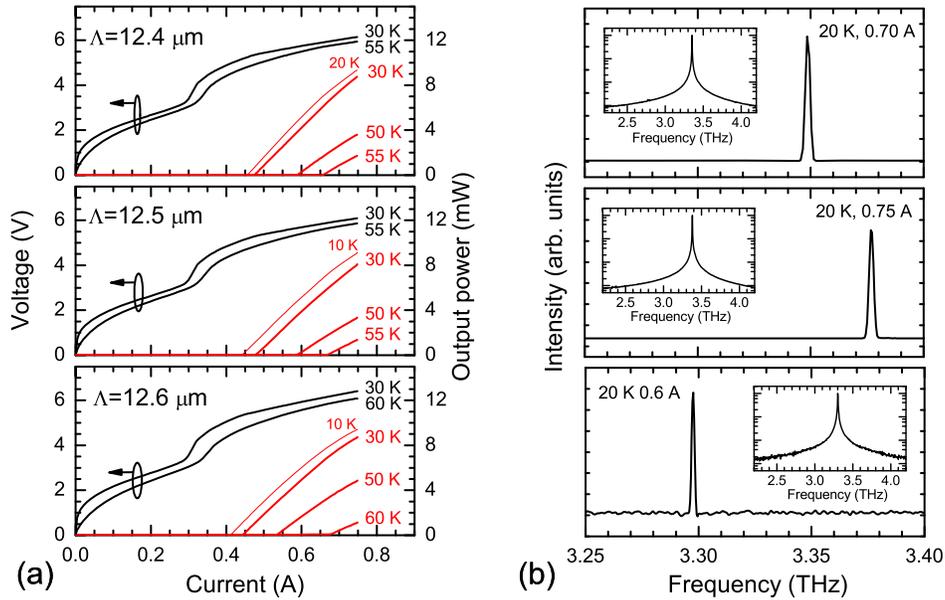
Fig. 3. (a) Continuous-wave *L-I-V* characteristics of three lDFB QCLs (ridge length 1.454 mm) with grating periods of 12.4, 12.5, and 12.6 μm at different temperatures. The nominal temperature of 10 K is maintained only up to current values of 0.46 A. (b) Typical emission spectra of the three lasers in their single-mode regime (linear intensity scale). Insets: Corresponding power spectra on a logarithmic scale for a wide frequency range.

$\Lambda = 12.6$ μm. The slope efficiency at threshold (30 K) is approximately 30 mW/A for all three lasers. The output powers at a driving current of 0.75 A are 8.7, 8.0, and 8.7 mW at 30 K and 3.6, 3.3, and 4.8 mW at 50 K for $\Lambda = 12.4$, 12.5, and 12.6 μm, respectively. For comparison, a Fabry-Pérot laser ridge of the same wafer with similar dimensions (0.10×1.52 mm^2) operated in cw mode up to 55 K. For this laser, values for the threshold current density, slope efficiency, and maximum cw output power at 30 K are 320 A cm^{-2}, 20 mW/A, and 6.5 mW, respectively. The smaller threshold current densities of the lDFB QCLs in comparison with Fabry-Pérot QCLs are qualitatively explained by a smaller threshold gain as a consequence of the feedback provided by the grating in addition to the feedback of the reflective end facets. However, the effect is stronger than expected. While the levels of cw output power are comparable for lDFB and Fabry-Pérot laser ridges, the spectral power density for the lDFB QCLs is much higher due to single-mode operation.

Figure 3(b) shows typical spectra of the three lasers in their respective single-mode regime. The side-mode suppression ratio exceeds the signal-to-noise ratio of 20–30 dB, which is limited by the baseline of the used Fourier-transform spectrometer and the QCL intensity. No side-modes could be detected within the entire current and temperature range of Fig. 3(a) for the laser with $\Lambda = 12.5$ μm. For the lasers with $\Lambda = 12.4$ (12.6) μm, this regime extends up to 0.7 (0.6) A at 20 K and over the entire driving current range at elevated temperatures (> 50 K). The single-mode emission for $\Lambda = 12.4$, 12.5, and 12.6 μm occurs at frequencies of 3.35, 3.38, and 3.30 THz, respectively. The single-mode tuning with driving current and temperature is limited to about 5 GHz for each laser, which is related to the rather small temperature dependence of the dielectric constants at low temperatures. The line width of the laser emission, which can be as
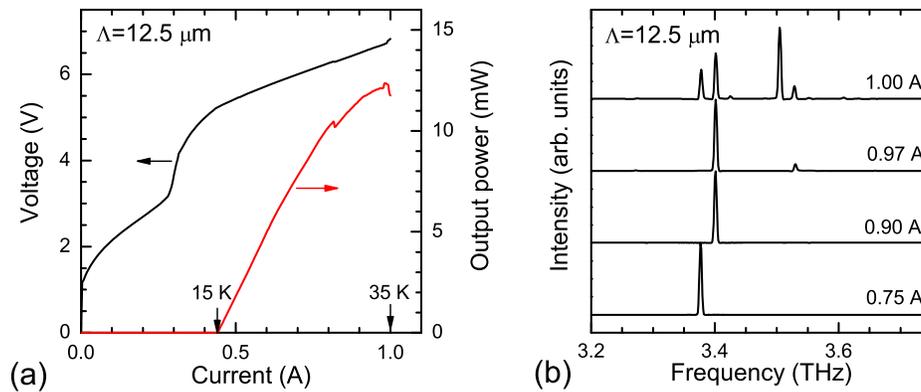
Fig. 4. (a) Continuous-wave *L-I-V* characteristics for the lDFB QCL with $\Lambda = 12.5\ \mu$m including the multi-mode emission regime (disabled temperature control loop). (b) Corresponding emission spectra at four different driving currents.

small as a few kHz for THz QCLs [26], cannot be determined from the spectra due to the limited resolution of the used spectrometer (Bruker, IFS66v). The instrumental resolution allows for a clear identification of modes, which are separated by more than 3.5 GHz. The question may arise, if these spectra consist of different transverse modes which are not resolved. However, we disregard this possibility for a simple reason. According to the simulation results discussed above, the effective index for the TM_{00} and TM_{01} mode differ by 1.2%, which causes a shift of the Bragg frequency from 3.33 to 3.37 THz. Hence, the longitudinal mode with the lowest threshold gain is expected to differ by more than 40 GHz for TM_{00} and TM_{01} symmetry, which is well beyond the resolution limit. In contrast, higher-order transverse modes are likely to explain the complicated multi-mode emission spectra observed at elevated driving currents.

From beam-profile measurements for one of the lDFB lasers operated in a Stirling cooler, we found that the far field is very similar to single-plasmon lasers without a grating (cf. Ref. [6]). For a driving current of 600 mA and operating temperature of 50 K, the beam profile of the $\Lambda = 12.4\ \mu$m laser consists mainly of a single lobe, covering approximately 80% of the power, for which we estimate a full width at half maximum divergence of about $24°$ in both, the lateral and the vertical, directions. The beam divergence appears to be comparable to the one of third-order DFB QCLs, for which values of 15 to $30°$ have been reported [16].

In Fig. 4(a), the *L-I-V* characteristics are shown for the laser with $\Lambda = 12.5\ \mu$m including the multi-mode emission regime. Due to the large dissipated electrical power at elevated current levels, the temperature control loop was disabled for this measurement resulting in a linear temperature increase of 20 K between the threshold and the maximum applied current of 1.0 A. At its maximum, the cw output power exceeds 12 mW for this laser. In Fig. 4(b), the emission spectra for different operating currents are shown. Between 0.75 and 0.9 A, the laser emission switches from 3.38 to 3.40 THz. This new regime is related to a discontinuity at 0.82 A in the light-current characteristics, which is also observed in the *I-V* characteristics. When the driving current is increased to 0.97 A, another mode at 3.53 THz starts to appear, and, at a driving current of 1.0 A, the laser emission exhibits a complex multi-mode pattern with strong modes at 3.38/3.40 THz and 3.50/3.53 THz.

The emission spectra can be interpreted within the framework of the coupled-mode equations for a DFB cavity (see Appendix) with the boundary condition of two reflective end facets, for which the facet phases as defined in Fig. 1(a) enter the eigenvalue problem. The coupled-mode
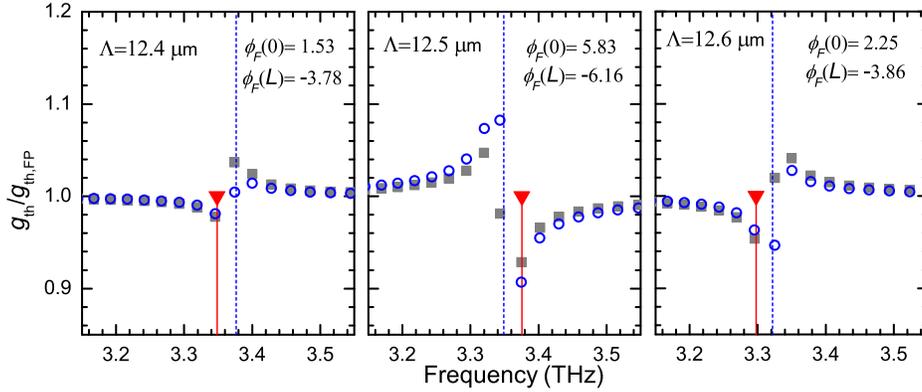
Fig. 5. Calculated threshold gain g_{th} vs. frequency of the eigenmodes of the lDFB lasers ($\Lambda = 12.4$, 12.5, and 12.6 μm) in units of g_{th} of the reference Fabry-Pérot cavity. The vertical dashed lines indicate the Bragg frequency using $n = 3.58$. The facet phases ϕ_F as defined in Fig. 1(a) have been determined by SEM imaging and are given in radians. Circles refer to a complex coupling coefficient [$K + iK_g = (3.0 + 0.8i)$ cm^{-1}] and squares to a real coupling coefficient ($K = 3.0$ cm^{-1}). Triangles indicate the experimentally observed frequencies.

equations have been solved numerically for this case. In Fig. 5, the calculated threshold gain for the TM$_{00}$ mode is plotted versus the frequency eigenvalues for the three lDFB QCLs with $\Lambda = 12.4$, 12.5, and 12.6 μm. We have performed simulations either for a complex coupling coefficient or for a real coupling coefficient ($K_g = 0$). The experimentally observed single-mode emission and the calculated longitudinal modes with the lowest threshold gain occur at almost the same frequencies, where the quantitative agreement appears to be better for the simulations with a real coupling coefficient. In this case, an agreement better than 9 GHz is found for all three lasers, while in the case of a complex coupling coefficient the calculated mode with the second lowest threshold gain coincides with the lasing frequency for $\Lambda = 12.6$ μm. While the Bragg frequency (depicted as dashed lines in Fig. 5) decreases with increasing grating period, the finite facet reflectance and the different facet phases cause lasing in the longitudinal mode below the Bragg frequency for $\Lambda = 12.4$ and 12.6 μm and above the Bragg frequency for $\Lambda = 12.5$ μm. The differences in the calculated threshold gain explain the different experimentally observed threshold current densities. However, the calculation predicts the lowest threshold gain for $\Lambda = 12.5$ μm, while experimentally the lowest value of J_{th} is found for $\Lambda = 12.6$ μm [cf. Fig. 3(a)]. Differences between the experimental and simulated results are likely due to the uncertainty of the involved parameters such as the coupling coefficients. For instance, the occurrence of a small displacement between the etch mask and the metallization mask might result in a phase difference between the index and gain coupling, which has been neglected in the simulations.

While the single-mode operation regime is quite well explained by the coupled-mode equations for the fundamental lateral TM$_{00}$ mode, the situation becomes more complex for the multi-mode emission regime. In Fig. 4(b), the emission of a second mode at 3.40 THz for the laser with $\Lambda = 12.5$ μm can be understood by the Stark shift of the gain with increasing bias, since the emission frequency agrees with the calculated frequency of the mode with the second lowest threshold gain. However, the multi-mode emission pattern for the highest driving current seems to exhibit a stop band between 3.40 and 3.50 THz. This cannot be explained by the

spectral position and threshold gain of the longitudinal modes with TM_{00} symmetry. A likely explanation is the presence of higher-order lateral modes such as TM_{01} and TM_{02}, for which the coupling coefficient is much larger and the Bragg frequency is increased due to the smaller effective index of these modes. For lasing of higher-order lateral modes in favor of the fundamental TM_{00} mode, the threshold gain has to be smaller as compared to the TM_{00} mode, i.e. the larger coupling coefficient has to compensate the higher waveguide losses.

4. Summary and conclusions

We have demonstrated THz QCLs based on first-order lateral DFB gratings and single-plasmon waveguides, which operate in continuous-wave mode with high output powers and single-mode emission around 3.3 THz. For the single-mode regime, cw output powers exceeding 8 mW have been obtained, while the maximum output power including the multi-mode regime can exceed even 12 mW. A method has been developed to calculate the coupling strength of DFB gratings in the presence of corrugated metal layers, which demonstrates that the origin of the large coupling strength in the investigated lasers is the strong plasmonic metal-light interaction at the lateral grating edges. The emission frequency of the lasers is determined by the Bragg frequency of the grating and the positions of the cleaved facets with respect to the grating comb. By taking into account the reflective end facets, a quantitative agreement between the experimental spectra and simulations based on the coupled-mode equations of DFB lasers is obtained. The present approach is limited by the accuracy of the cleaving process, which causes an uncertainty of the emission frequency approximately equal to the mode spacing of the corresponding Fabry-Pérot cavity. However, the number of mounted laser dies, which have to be tested to obtain a particular target frequency, can be kept small if laser ridges with different grating periods are located on the same die.

5. Appendix

In order to derive Eq. (1), we start with the coupled-mode equations following the notation of Ref. [21]:

$$\frac{d}{dz}\begin{pmatrix} A(z) \\ B(z) \end{pmatrix} = i \begin{pmatrix} \Delta\beta & K_{ab} \\ -K_{ba} & -\Delta\beta \end{pmatrix} \begin{pmatrix} A(z) \\ B(z) \end{pmatrix}. \tag{4}$$

$A(z)$ and $B(z)$ denote the amplitudes of the forward and backward propagating wave, respectively. K_{ab} and K_{ba} refer to the coupling coefficients of the forward and backward propagating mode, respectively, and $\Delta\beta = \beta_0 - \beta_B$ corresponds to the difference of the propagation constant $\beta_0 = \omega n_{\text{eff}}/c$ and the Bragg wavevector $\beta_B = \pi/\Lambda$. The coupled-mode equations in Eq. (4) are formally solved by

$$\begin{pmatrix} A(z) \\ B(z) \end{pmatrix} = \begin{pmatrix} A_\pm \\ B_\pm \end{pmatrix} e^{\pm iqz} \tag{5}$$

with

$$q = \sqrt{\Delta\beta^2 - K_{ab}K_{ba}}. \tag{6}$$

The latter equation is the dispersion relation for the coupled system of forward and backward propagating waves of a uniform grating of infinite length. The propagation constant of the coupled system are given by $\beta_\pm = \pi/\Lambda \pm q$, while β_0 and $\Delta\beta$ refer to the reference waveguide. Note that q, β_0, and $\Delta\beta$ are complex quantities in the current notation due to the presence of gain and losses, while the frequency ω is a real quantity.

In the case of index and gain coupling, the coupling coefficients can be written as $K_{ab} = K + iK_g \exp(i\phi_g)$ and $K_{ba} = K + iK_g \exp(-i\phi_g)$ with K denoting the index coupling coefficient,

K_g the gain coupling coefficient, and ϕ_g the phase difference between index and gain coupling. We obtain the relation

$$K_{ab}K_{ba} = K^2 - K_g^2 + 2iKK_g\cos(\phi_g) \ . \tag{7}$$

Here, only symmetric gratings are considered, for which the origin in the ridge direction z can be chosen such that $\Delta\varepsilon(z) = \Delta\varepsilon(-z)$. The only possible values for ϕ_g are 0 and π, $K_{ab}K_{ba} = (K \pm iK_g)^2$, where we chose the plus sign in the following by allowing for negative amplitudes K_g. We rewrite Eq. (6) using $\omega = \beta_0 c/n_{\text{eff}} = \beta_0 c/(n+ik)$:

$$\omega_\pm(q) = \frac{c}{n+ik}\left(\frac{\pi}{\Lambda} \pm \sqrt{q^2 + K_{ab}K_{ba}}\right) \ . \tag{8}$$

In the following, the wavevector $\pi/\Lambda \pm q$ is treated as a real quantity, which causes β_0 and $\Delta\beta$ to be real, while the frequency ω becomes complex. The case $q = 0$ correspond to the eigenfrequencies of a one-dimensional photonic crystal at the edge of the Brillouin zone. Assuming a symmetric grating with $K_{ab}K_{ba} = (K+iK_g)^2$, the complex frequencies of the two eigenmodes at $q = 0$ are given by Eq. (1).

Acknowledgment